

Broadband Nonreciprocity Realized by Locally Controlling the Magnon's Radiation

Y.T. Zhao, J.W. Rao[✉],* Y.S. Gui, Y.P. Wang[✉], and C.-M. Hu[†]

Department of Physics and Astronomy, University of Manitoba, Winnipeg R3T 2N2, Canada



(Received 28 March 2020; revised 30 May 2020; accepted 2 June 2020; published 13 July 2020)

Interference between coherent and dissipative coupling results in nonreciprocity in cavity magnonic devices, in which the isolation ratio can theoretically be infinite when the magnon-mode frequency exactly matches a zero-damping condition (ZDC). In order to obtain a nonreciprocal device possessing both a high isolation ratio and a broad operating bandwidth, we tune the side ZDCs by integrating a movable loop antenna, which can effectively control the radiation damping of the magnon mode. As a consequence, the effective operating bandwidth of the giant nonreciprocity can be broadened to a few hundred times the magnon linewidth. Our study offers a feasible method to design a broadband nonreciprocal device with a high isolation ratio by engineering photon-magnon coupling, which may be of benefit for future quantum and coherent information processing.

DOI: [10.1103/PhysRevApplied.14.014035](https://doi.org/10.1103/PhysRevApplied.14.014035)

I. INTRODUCTION

In quantum information processing, fast readout of a long-lifetime qubit requires delicate isolation and shielding between the qubit and the circuit [1–4]. This remains a great challenge [4–9] because even a tiny amount of energy leakage would spoil the sensitive quantum state [1]. Given this fact, nonreciprocal devices [10] that can unidirectionally shield qubits are much needed. Several mechanisms have been put forward for producing nonreciprocity with a high isolation ratio, such as Faraday rotation [11], reservoir engineering [12,13], optomechanical interactions [14,15], active dynamics [16], and chiral modes [17]. Very recently, an alternative approach has been demonstrated [18] using cavity magnonics [19–30], in which one manipulates the interference between coherent [29–35] and dissipative [36–44] coupling. Unlike previous methods, infinite isolation in such a cavity magnonic device is theoretically achievable, which makes it suitable for protecting sensitive quantum states.

Specifically, dissipative coupling in a cavity magnonic device allows one to create two zero-damping conditions (ZDCs) [18,45], under which a hybridized mode with zero intrinsic damping is produced, corresponding to complete blocking of microwave transmission. Because the interference term between coherent and dissipative coupling changes sign between the cases of forward and backward transmission [18], the two ZDCs for forward transmission are staggered in the frequency domain with respect to those for backward transmission. As a consequence, giant

nonreciprocity occurs when the magnon-mode frequency approaches any of these four ZDCs.

While the isolation ratio of these nonreciprocal devices can theoretically be infinite, the operating bandwidth for the giant nonreciprocity is limited by the resonance linewidth. From the perspective of practical applications, a nonreciprocal device that possesses both infinite isolation and a wide bandwidth is much more desirable than one with infinite isolation at only four single frequencies. To achieve such a goal, we propose a method to broaden the effective nonreciprocal bandwidth of a cavity magnonics device. Experimentally, a small loop antenna is integrated to control the radiative damping of the magnon mode [46]. As a result, the side ZDCs of our device can be tuned over a wide frequency range, a few hundred times broader than the linewidth of the magnon mode. By means of this method, the effective bandwidth of the giant nonreciprocity at the side ZDCs is broadened to up to approximately 200 MHz. Our study demonstrates a feasible technical solution to the problem of broadening the bandwidth of a giant-nonreciprocal device based on cavity magnonics, which may be of benefit for the design of practical nonreciprocal devices for future quantum technology.

II. EXPERIMENTAL RESULTS

Figure 1(a) shows a schematic diagram of the interactions between a cavity photon mode and a magnon mode. Both of these modes are side-coupled to an impedance-matched transmission line. ω_c and ω_m are their uncoupled mode frequencies. κ and γ represent their respective extrinsic dampings due to the coupling with the transmission line. Because of the correlation of these two radiative

*jinweir@myumanitoba.ca

†hu@physics.umanitoba.ca

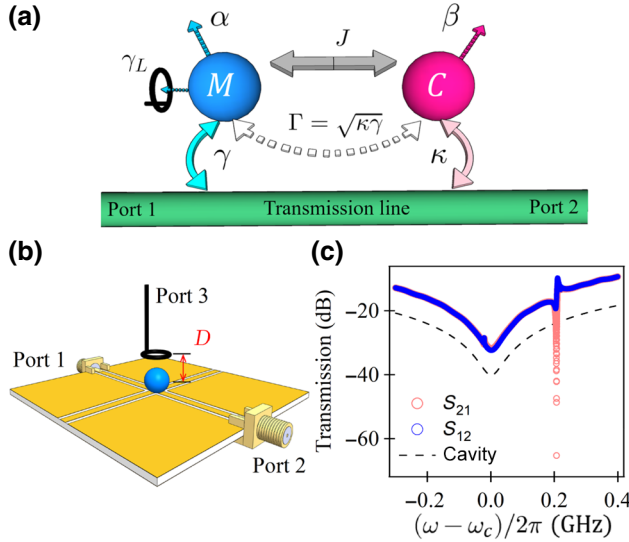


FIG. 1. (a) Schematic diagram of the interactions between a magnon mode and a cavity mode. A loop antenna is placed close to the magnon mode to control its radiation. (b) Schematic picture of our device. An yttrium iron garnet (YIG) sphere is placed at the intersection of a cross-shaped cavity. The separation distance D between the YIG sphere and the loop antenna is tunable. (c) Comparison of the forward and backward transmission spectra ($|S_{21}|$ and $|S_{12}|$) measured at a side ZDC. The black dashed line indicates the measured transmission spectrum of the empty cavity, which is shifted by -10 dB for the sake of clarity.

dampings, an indirect coupling effect is produced between the two modes with a strength of $i\Gamma = i\sqrt{\kappa\gamma}$. Notice that the coupling strength is imaginary, which indicates that this indirect coupling is purely dissipative. In addition, due to the direct overlap of the modes, a coherent coupling effect with a strength of J also exists. β and α represent the intrinsic damping rates of the cavity photon mode and the magnon mode, respectively; these damping rates have no obvious effect on the interactions between the two modes. A loop antenna is placed close to the magnon mode to introduce an additional radiation damping rate (γ_L) of the magnon mode.

To describe the dynamics of this hybrid system, an effective Hamiltonian is constructed (Appendix A), from which the transmission spectrum of the system in the forward and backward directions can be derived as

$$S_{21(12)} = 1 + \frac{\kappa}{i(\omega - \omega_c) - \kappa - \beta + \frac{(J - i\Gamma e^{i\Theta_{1(2)}})^2}{i(\omega - \omega_m) - \alpha'}} \quad (1)$$

where $\Theta_{1(2)}$ is used to indicate the different interference behaviors of the two types of coupling effects, and can be 0 or π for a microwave signal loaded from port 1 or port 2, respectively. α' represents the total damping rate of the magnon mode, which includes the Gilbert damping (α),

the radiation damping into the transmission line (γ), and the radiation damping into the loop antenna (γ_L). The complex frequencies of the two hybridized modes of the system can be solved for, and the result is $\tilde{\omega}_{\pm} = [\tilde{\omega}_c + \tilde{\omega}_m \pm \sqrt{(\tilde{\omega}_c - \tilde{\omega}_m)^2 + 4(J - i\Gamma e^{i\Theta_{1(2)}})^2}]/2$, where $\tilde{\omega}_c = \omega_c - i\beta$ and $\tilde{\omega}_m = \omega_m - i\alpha'$ are the complex resonance frequencies of the cavity photon and magnon modes.

From $\text{Im}(\tilde{\omega}_{\pm}) = 0$, the mathematical expressions for the two ZDCs can be approximated to first order by the following detunings (where $\Delta = \omega_c - \omega_m$):

$$\begin{aligned} \Delta_{ce} &= -\frac{2J\Gamma e^{i\Theta_{1(2)}}}{\beta} + \frac{(\alpha' + \beta)(J^2 - \Gamma^2 + \alpha'\beta)}{2J\Gamma e^{i\Theta_{1(2)}}}, \\ \Delta_{si} &= \frac{2J\Gamma e^{i\Theta_{1(2)}}}{\alpha'} - \frac{(\alpha' + \beta)(J^2 - \Gamma^2 + \alpha'\beta)}{2J\Gamma e^{i\Theta_{1(2)}}}, \end{aligned} \quad (2)$$

where $\Delta_{ce} = \omega_{m,ce} - \omega_c$ and $\Delta_{si} = \omega_{m,si} - \omega_c$ are the central and side ZDCs, respectively, according to whether their frequency is close to or away from the matched resonance condition $\omega_m = \omega_c$. $\omega_{m,ce}$ and $\omega_{m,si}$ are the magnon-mode frequencies corresponding to the center and side ZDCs, respectively. As the Q factor of one hybridized mode is infinite, the ZDCs can potentially be used in sensing technologies. Specifically, the ultrasharp mode at the central ZDC is sensitive to perturbations of the microwave electric field near the cavity, while the ultrasharp mode at the side ZDC is sensitive to perturbations of the microwave magnetic field near the YIG sphere. By utilizing their distinct dynamic properties, one could use the proposed cavity magnonic device to sense both the permittivity and the permeability of materials.

Equation (2) shows that the ZDCs also depend on the phase Θ (or the direction of microwave propagation), and therefore four ZDCs should exist in our cavity magnonic device, in general. When the magnon-mode frequency (ω_m) approaches one of them, the input signal is completely blocked in one transmission direction but can propagate freely through the device in the other transmission direction. Since the central ZDCs are very close to the cavity mode (which has a very large extrinsic damping rate), these ZDCs inevitably lead to a larger insertion loss than do the side ZDCs [18]. Based on this fact, we can conclude that the side ZDCs are more favorable for achieving giant nonreciprocity in practical applications.

The tunability of both the central and the side ZDCs is clearly seen in Eq. (2): besides the two coupling strengths (J and Γ), they can also be tuned by means of the damping rates (β and α'). Here we design an experiment to demonstrate the controllability of the side ZDCs using a movable loop antenna. As a consequence, giant nonreciprocity with an effectively broad bandwidth is achieved.

Our experimental setup is shown in Fig. 1(b), and consists of three main parts: a planar cross-shaped cavity, an YIG sphere, and a loop antenna. The planar cross-shaped

cavity is fabricated on an RO4350B TM substrate with a thickness of 0.85 mm. It is an open system and can sustain both traveling and standing waves (cavity modes). An YIG sphere with a diameter of 1 mm is placed at the intersection of the cross to produce coupling effects with the cavity. An external magnetic field produced by an electromagnet is applied vertically to saturate the magnetization of the YIG sphere and control the magnon-mode frequency ω_m linearly. To achieve a strong coupling effect, the uniform Kittel mode of the YIG sphere is chosen, which entails a large net magnetic dipole moment [8]. Above the sphere, a loop antenna is used to introduce additional radiation damping of the magnon mode (γ_L). The loop antenna is fixed to a motor-driven stage and can be moved vertically in a range of 0.5–6.5 mm. Because the side ZDCs of our device are sensitive to the damping rate of the magnon mode [α' in Eq. (2)], even a small perturbation from the loop antenna can result in an evident frequency shift of the side ZDCs.

Firstly, we characterize the giant nonreciprocity at a side ZDC. Figure 1(c) shows the measured results. The cavity mode occurs at $\omega_c/2\pi = 5.8$ GHz, shown by the black dashed line. Its intrinsic and extrinsic damping rates are extracted from fitting of the curve as $\beta/2\pi = 32.6$ MHz and $\kappa/2\pi = 1.3$ GHz. If the external magnetic field is set to 233 mT to make the detuning equal to Δ_{si} , the side ZDC for forward transmission (S_{21}) is satisfied. Besides the cavitylike hybridized mode near ω_c , an ultrasharp dip (magnonlike mode) occurs at $\omega_+/2\pi = \omega_c/2\pi + 0.2$ GHz, which indicates that the input signal is nearly completely blocked [red circles in Fig. 1(c)]. However, for backward transmission (S_{12}) at the same magnetic field, the side ZDC is not satisfied, because of the phase change in the dissipative coupling term, so that a small resonant dip occurs instead of an ultrasharp dip. The giant nonreciprocity occurs at $\omega = \omega_+$, with an isolation ratio $[20|\log_{10}(S_{21}/S_{12})|]$ greater than 50 dB.

We demonstrate a method to tune the side ZDCs by moving the loop antenna, to obtain such a giant nonreciprocity over a wide frequency range. Figure 2 shows the measurement results. At the beginning, the loop antenna is placed above the YIG sphere at a separation of 0.55 mm. Forward transmission spectra (S_{21}) are measured and are plotted as a function of the frequency detuning $\omega - \omega_c$ and external magnetic field in Fig. 2(a). Two sharp resonances occur at (−67.9 MHz, 222 mT) and (178 MHz, 232 mT), which correspond to the ultrasharp modes at the central and side ZDCs, respectively. The measured dispersions of the two hybridized modes in our device are plotted in the middle panel between Figs. 2(a) and 2(b), from which the two coupling strengths between the cavity mode and the magnon mode are fitted as $J/2\pi = 6.5$ MHz and $\Gamma/2\pi = 29$ MHz. Since the dissipative coupling effect is more dominant than the coherent coupling, i.e., $|\Gamma| > |J|$, the dispersions of the two hybridized modes exhibit a typical

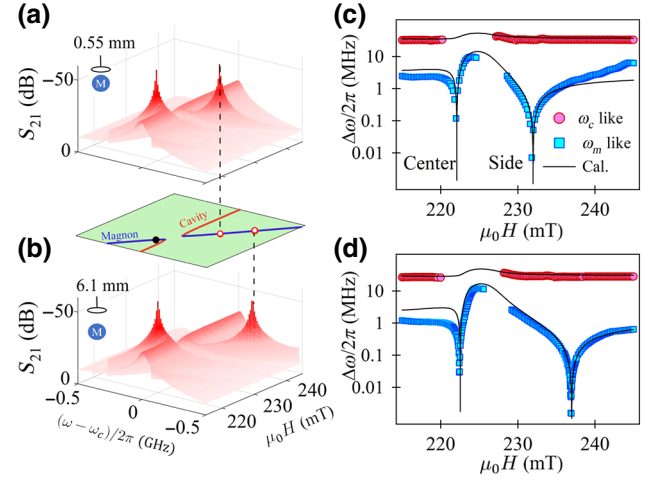


FIG. 2. (a),(b) Measured forward transmission spectra plotted as a function of the detuning $[(\omega - \omega_c)/2\pi]$ and the external magnetic field. For the sake of clarity, the z axes of the two three-dimensional (3D) plots are reversed. The two sharp resonances indicate the ultrasharp modes that occur at ZDCs. The two insets depict the separation between the loop antenna and the YIG sphere during the measurement. The middle panel shows the dispersions of the two hybridized modes in our cavity magnonic device. The blue and red solid lines represent the magnonlike and cavitylike hybridized modes, respectively. The black dot indicates the central ZDC, which stays the same in the two different measurements. The red circles indicate the ultrasharp modes at the side ZDCs, which can be shifted by the loop antenna. (c),(d) Linewidths of the two hybridized modes fitted to the measured transmission spectra. The blue and red symbols represent the linewidths of the magnonlike and cavitylike hybridized modes, respectively. The solid lines show the calculated values of $|\text{Im}(\tilde{\omega}_{\pm})|$, which are the intrinsic damping rates of the two hybridized modes.

level attraction [37]. The central and side ZDCs are marked by a black dot and red circles, respectively, in this plane.

For comparison, we also measure the forward transmission spectra with the loop antenna separated from the YIG sphere by a distance of 6.1 mm [Fig. 2(b)]. In this case, the dispersions of the two hybridized modes remain the same as in the former case, which indicates that the loop antenna has a negligible effect on the effects of coupling between the cavity photon mode and the magnon mode. The central ZDC of our device shows negligible change at (−67.2 MHz, 222 mT), but the side ZDC is obviously shifted from (178 MHz, 232 mT) to (305 MHz, 237 mT). The linewidths of the two hybridized modes in both cases are extracted from the measured transmission spectra, and are plotted in Figs. 2(c) and 2(d). Evidently, the two dips for the magnonlike mode [blue symbols in Figs. 2(c) and 2(d)] are related to the ZDCs. A comparison between the two cases clearly shows the influence of the loop antenna on the side ZDCs. In addition, the black solid lines show

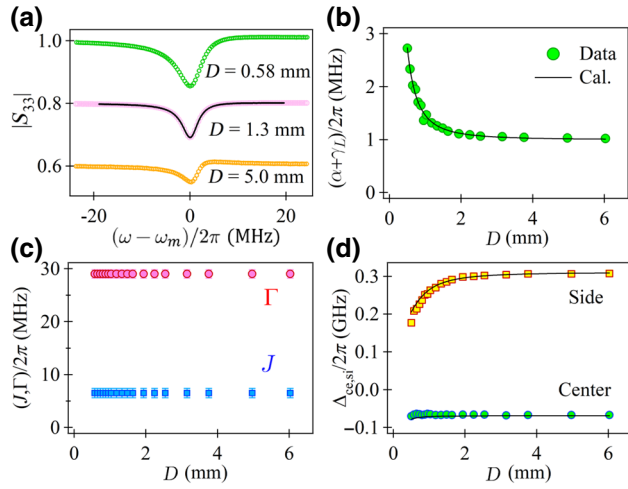


FIG. 3. (a) Three reflection spectra measured from the loop antenna at separations of 0.58, 1.3, and 5.5 mm. The reflection spectra measured at 1.3 and 5 mm are shifted downwards by 0.2 and 0.4, respectively. The black solid line is the result of a calculation using Eq. (C2). (b) Damping rate of the magnon mode fitted to the spectra in (a), which exhibits an inverse-square dependence on the separation (D). The black solid line is a D^{-2} curve to guide the eye. (c) Coherent (J) and dissipative (Γ) coupling strengths at different separations D , extracted from the measured dispersions of the two hybridized modes, which are independent of D . (d) Two ZDCs as a function of D . The symbols and black solid lines indicate the experimental data and the results of calculations using Eq. (2).

the calculated imaginary part of $\tilde{\omega}_{\pm}$, which can describe our experimental results well.

The loop antenna in our device works like a port locally coupled to the magnon mode, which offers the magnon mode an additional dissipation channel. The additional dissipation (γ_L) depends strongly on the separation between the loop antenna and the YIG sphere. To obtain a quantitative dependence on the separation (D),

we perform another measurement to detect the reflection spectrum of the magnon mode from the loop antenna, i.e., S_{33} . Figure 3(a) shows three typical reflection spectra measured at different separations. The resonant dip represents the magnon mode of the YIG sphere, which exhibits an evident dependence on the separation. The total damping rate, including the Gilbert damping (α) and the radiation damping induced by the loop antenna (γ_L), obtained by curve fitting of the measured reflection spectra using Eq. (C2), is plotted in Fig. 3(b); it exhibits an inverse-square dependence on the separation (D), i.e., $\alpha + \gamma_L \propto D^{-2}$. Approximately, the YIG sphere can be viewed as a point source. With an increase in the separation, the solid angle of the loop antenna relative to the YIG sphere decreases with an inverse-square dependence [47], which results in the D^{-2} variation of γ_L .

For each separation of the loop antenna, the forward transmission spectra (S_{21}) are measured, from which the coupling strengths (Γ and J) and the two ZDCs ($\Delta_{ce,si}$) are extracted; these are plotted in Figs. 3(c) and 3(d). Consistent with the results shown in Fig. 2, the coupling strengths remain constant when the loop antenna is moved. The central ZDC ($\Delta_{ce}/2\pi$) also remains constant, but the side ZDC ($\Delta_{si}/2\pi$) can be tuned from 150 MHz to 300 MHz. The black solid lines in Fig. 3(d) show the results calculated using Eq. (2) considering the dependence of γ_L , which describe the variation of the two ZDCs very well. These results indicate that the loop antenna has a significant influence on the damping rate of the magnon mode, but has a negligible effect on the cavity photon mode.

In the experiment described next, we demonstrate how to achieve an effective broadband giant nonreciprocity in a cavity magnonic device by shifting the side ZDCs. Figure 4(a) shows the measured isolation ratio of our device at $D = 0.55$ mm. The four sharp peaks in the 3D plot indicate giant nonreciprocity at four ZDCs. For each isolation peak, the effective bandwidth of the nonreciprocity for an isolation ratio greater than 20 dB is only 2

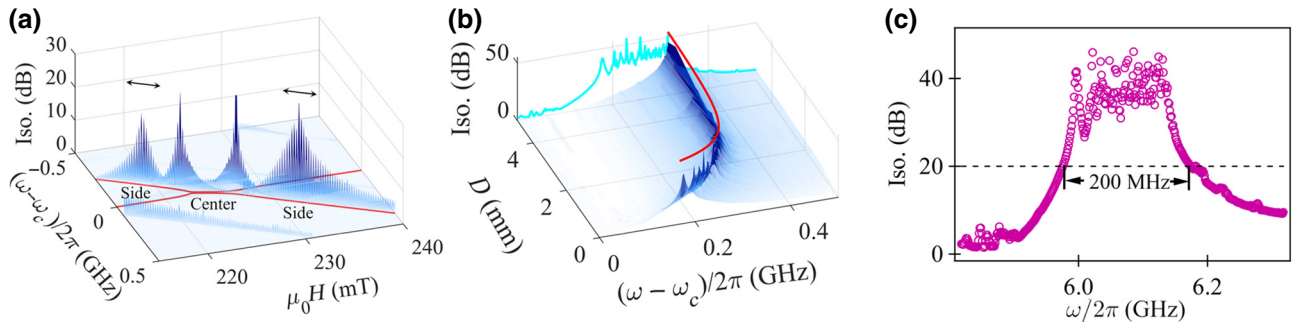


FIG. 4. (a) Isolation ratio (Iso.) of our device measured at $D = 0.55$ mm. The red solid lines indicate the calculated dispersions of the two hybridized modes. (b) Isolation peak at the side ZDC at a higher frequency than the cavity-mode frequency shifted by the loop antenna. The red solid line indicates the frequency shift of the isolation peak. The blue solid line indicates the projection of the giant nonreciprocity at the side ZDC onto the x - z plane. To emphasize this giant nonreciprocity, we plot this effectively broadband nonreciprocity (approximately 200 MHz) in (c).

MHz, which limits the practical use of our nonreciprocal device. As demonstrated above, the two side ZDCs can be shifted by means of the loop antenna over a wide range, so that the corresponding nonreciprocities at these two side ZDCs are tunable. As an example, we choose the side ZDC at (178 MHz, 232 mT) in Fig. 4(a), and measure the frequency shift of the isolation peak [Fig. 4(b)]. When the separation D is increased from 0.5 to 5.5 mm, the isolation peak is shifted to a higher frequency by an amount of 150 MHz. This indicates that giant nonreciprocity is achievable in this tunable frequency range, as long as the separation D and the magnetic field are matched. Assuming that the cavity-mode frequency is 5.8 GHz, the effective band of the giant nonreciprocity is from 5.95 GHz to 6.15 GHz [Fig. 4(c)]. Besides the side ZDC at a higher frequency than the cavity-mode frequency, the side ZDC at a lower frequency (−178 MHz, 219 mT) can produce another giant-nonreciprocity band as a result of tuning the separation of the loop antenna (not shown in the figure).

III. CONCLUSIONS

In this paper, we experimentally demonstrate enhancement of the nonreciprocal bandwidth of a cavity magnonic device by locally controlling the magnon's radiation. We find that the side ZDCs of our device are more sensitive to the damping rate of the magnon mode. Accordingly, a loop antenna is placed close to the YIG sphere of the device, and this antenna works as an additional dissipation channel for the magnon mode. By changing the separation between it and the YIG sphere, the radiation from the magnon mode to the loop antenna can be controlled, so that the side ZDCs of our device can be shifted over a wide frequency range of a few hundred times the magnon linewidth. By means of this property, an effective broadband giant nonreciprocity is achieved, which has a width of approximately 200 MHz. At present, nonreciprocal devices with both a high isolation ratio and a broad bandwidth are much needed in the thriving field of quantum technology. Our results may further these efforts by providing a feasible method to achieve broadband giant nonreciprocity based on cavity magnonics. Such nonreciprocal devices can be

used to unidirectionally shield a qubit, so that quantum information can be read out from the qubit, but meanwhile the thermal and charge fluctuations in the readout circuit are completely blocked.

ACKNOWLEDGMENTS

This work was funded by NSERC Discovery Grants and NSERC Discovery Accelerator Supplements (C.-M.H.). Y. T. Zhao is supported by a University of Manitoba Graduate Fellowship. J.W.R. is supported by a CSC scholarship. We would like to acknowledge CMC Microsystems for providing equipment that facilitated this research.

APPENDIX A: EFFECTIVE HAMILTONIAN OF OUR CAVITY MAGNONIC DEVICE

To model the dynamics of our cavity magnonic device, an effective Hamiltonian is constructed according to Ref. [18]:

$$\hat{H}_e/\hbar = \tilde{\omega}_c \hat{a}^\dagger \hat{a} + \tilde{\omega}_m \hat{b}^\dagger \hat{b} + (J - ie^{i\Theta_{1(2)}} \Gamma)(\hat{a}^\dagger \hat{b} + \hat{a} \hat{b}^\dagger), \quad (\text{A1})$$

where \hat{a} (\hat{a}^\dagger) and \hat{b} (\hat{b}^\dagger) represent the annihilation (creation) operators of the cavity photon and magnon modes, respectively. $\Theta_{1(2)}$ is 0 or π for microwave signals loaded from port 1 or 2.

In the absence of external driving sources, according to Eq. (A1), the evolution of the two coupled modes in time can be derived as

$$\frac{d}{dt} \begin{bmatrix} \hat{a} \\ \hat{b} \end{bmatrix} = -i \begin{bmatrix} \tilde{\omega}_c & J - i\Gamma e^{i\Theta_{1(2)}} \\ J - i\Gamma e^{i\Theta_{1(2)}} & \tilde{\omega}_m \end{bmatrix} \begin{bmatrix} \hat{a} \\ \hat{b} \end{bmatrix}. \quad (\text{A2})$$

From this dynamic equation, the dispersions of the two hybridized modes can be obtained as $\tilde{\omega}_\pm = [\tilde{\omega}_c + \tilde{\omega}_m \pm \sqrt{(\tilde{\omega}_c - \tilde{\omega}_m)^2 + 4(J - i\Gamma e^{i\Theta_{1(2)}})^2}]/2$. At two specific detunings (Δ_m), a hybridized mode with zero intrinsic damping rate occurs, because of the dissipative coupling effect. These two detunings are the so-called zero-damping conditions, and can be obtained by setting $\text{Im}(\tilde{\omega}_\pm) = 0$:

$$\Delta_m = \frac{(\beta - \alpha')J\Gamma e^{i\Theta_{1(2)}} \pm (\alpha' + \beta)\sqrt{J^2\Gamma^2 + \alpha'\beta(J^2 - \Gamma^2 + \alpha'\beta)}}{\alpha'\beta}, \quad (\text{A3})$$

where $\alpha' = \alpha + \gamma + \gamma_L$ is the total damping rate of the magnon mode. If $J^2\Gamma^2 \gg \alpha'\beta(J^2 - \Gamma^2 + \alpha'\beta)$, a concise form of these two ZDCs can be obtained by using the first-order approximation of the square-root term, i.e., Eq. (2).

APPENDIX B: TRANSMISSION SPECTRUM OF OUR MAGNONIC DEVICE

When the microwave signal is loaded from port 1 or 2, the dynamics of our magnonic device is governed by the

quantum Langevin equation

$$\frac{d}{dt} \begin{bmatrix} \hat{a} \\ \hat{b} \end{bmatrix} = -i \begin{bmatrix} \tilde{\omega}_c - i\kappa & J - i\Gamma e^{i\Theta_{1(2)}} \\ J - i\Gamma e^{i\Theta_{1(2)}} & \tilde{\omega}_m \end{bmatrix} \begin{bmatrix} \hat{a} \\ \hat{b} \end{bmatrix} + \begin{bmatrix} \sqrt{\kappa} \\ \sqrt{\gamma} \end{bmatrix} \hat{p}_{1(2)}^{\text{in}}, \quad (\text{B1})$$

where $\hat{p}_{1(2)}^{\text{in}}$ represents the input signal from port 1 or 2, which drives the cavity photon mode (\hat{a}) and the magnon mode (\hat{b}) simultaneously. Because $\kappa \gg \gamma$, the drive applied to the magnon mode, i.e., $\sqrt{\gamma} \hat{p}_{1(2)}^{\text{in}}$, can be neglected. For the same reason, the input-output relation of our device can be simplified to $\hat{p}_{2(1)}^{\text{out}} = \hat{p}_{1(2)}^{\text{in}} - \sqrt{\kappa} \hat{a}$, and the transmission spectrum can be derived as $S_{21(12)} = \langle \hat{p}_{2(1)}^{\text{out}} \rangle / \langle \hat{p}_{1(2)}^{\text{in}} \rangle$.

APPENDIX C: REFLECTION SPECTRUM MEASURED FROM THE LOOP ANTENNA

In our experimental setup, the loop antenna can be viewed as an additional port for the magnon mode. The radiation damping rate (γ_L) of the magnon mode induced by the loop antenna can be characterized by measuring the reflection spectrum (S_{33}). When the magnon-mode frequency is tuned away from the cavity photon mode (i.e., $|\Delta_m| \gg |J - i\Gamma e^{i\Theta_{1(2)}}|$), the influence of the cavity photon mode on the magnon mode can be neglected. Therefore, the dynamics of the magnon mode can be simply described by the Hamiltonian $\hat{H}_m/\hbar = [\omega_m - i(\alpha + \gamma)] \hat{b}^\dagger \hat{b}$. From this, the quantum Langevin equation of the magnon mode is

$$\frac{d\hat{b}}{dt} = -i[\omega_m - i(\alpha + \gamma)]\hat{b} - \frac{\gamma'}{2}\hat{b} + \sqrt{\gamma'}\hat{p}^{\text{in}}, \quad (\text{C1})$$

where γ' is the coupling strength between the magnon mode and the external photon bath. The radiation damping rate of the magnon mode induced by the loop antenna is $\gamma_L = \gamma'/2$. Adopting the input-output relation $\hat{p}^{\text{out}} = \hat{p}^{\text{in}} - \sqrt{\gamma'}\hat{b}$, the reflection spectrum of the magnon mode is derived as

$$S_{33} = 1 - \frac{\gamma'}{i(\omega_m - \omega) + (\alpha + \gamma + \gamma_L)}. \quad (\text{C2})$$

APPENDIX D: EQUIVALENT-CIRCUIT MODEL FOR THE DISSIPATIVE COUPLING EFFECT

Since our device works in a linear dynamic regime, besides the aforementioned quantum model, the coupling effects in it can also be described by an equivalent LCR circuit model. The coherent coupling effect between the cavity mode and the magnon mode can be described as a mutual capacitance and a mutual inductance between two LCR resonators, which has been well studied in previous

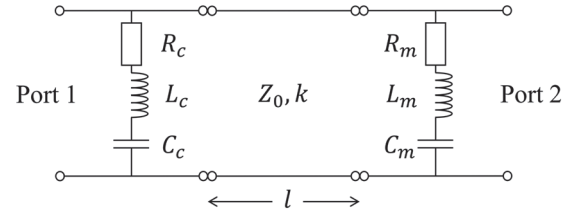


FIG. 5. Equivalent-circuit model for the dissipative coupling effect in our device. Two resonant LCR circuits represent the cavity resonance and the magnon-mode resonance; l is the separation of these two resonators. Z_0 and k are the characteristic impedance of the transmission line and the wave vector of traveling waves, respectively.

publications [48,49]. Here, we focus only on the dissipative coupling effect in cavity magnonics. As shown in Fig. 5, the cavity mode and the magnon mode are represented by two series LCR resonators. $R_{c(m)}$, $C_{c(m)}$, and $L_{c(m)}$ are the equivalent resistance, capacitance, and inductance, respectively, of the cavity (magnon) mode. The two resonators are connected to a common transmission line with a characteristic impedance of Z_0 , l is the separation of the two resonators, and k is the wave vector of traveling waves on the transmission line.

The scattering properties of this circuit can be described by cascaded matrices for the cavity mode, transmission line, and magnon mode, i.e., M_c , M_L , and M_m . The ABCD matrix of the whole circuit can be obtained by simply multiplying these three transmission matrices [48]:

$$\begin{bmatrix} A & B \\ C & D \end{bmatrix} = M_c M_L M_m = \begin{bmatrix} 1 & 0 \\ 1/Z_c & 1 \end{bmatrix} \begin{bmatrix} \cos kl & -iZ_0 \sin kl \\ -iZ_0^{-1} \sin kl & \cos kl \end{bmatrix} \begin{bmatrix} 1 & 0 \\ 1/Z_m & 1 \end{bmatrix}, \quad (\text{D1})$$

where $Z_{c(m)}$ is the impedance of the equivalent series resonator of the cavity (or magnon) mode, which has the form [48] $Z_{c(m)} = -i(L_{c(m)}/\omega)[\omega^2 - \omega_{c(m)}^2 + i2\omega(R_{c(m)}/2L_{c(m)})]$. Here, $\omega_{c(m)} = 1/\sqrt{L_{c(m)}C_{c(m)}}$ is the mode frequency of the cavity (magnon), and $R_{c(m)}/2L_{c(m)}$ represents the intrinsic damping rate of the cavity (magnon), i.e., β (α) in Eq. (1).

From the ABCD matrix, the transmission spectrum of the circuit can be derived as

$$S_{21} = \frac{2}{A + B/Z_0 + CZ_0 + D} \approx 1 + \frac{\kappa}{i(\omega - \omega_c) - (\beta + \kappa) + \frac{\kappa\gamma e^{i(2kl+\pi)}}{i(\omega - \omega_m) - (\alpha + \gamma)}}, \quad (\text{D2})$$

where $\kappa = Z_0/4L_c$ and $\gamma = Z_0/4L_m$ are the extrinsic damping rates of the cavity mode and magnon mode, respectively. Since $\kappa \gg \gamma$, we neglect the weak drive term acting on the magnonlike resonator, and get the concise form shown in Eq. (D2). Comparing this with Eq. (1), because of the cooperative effect between these two extrinsic damping rates, an indirect coupling effect with a strength of $\sqrt{\kappa\gamma}e^{i(2kl+\pi)}$ is produced. In the experiment, the YIG sphere is placed at the intersection of the cross-shaped cavity, so that $l = 0$ and the indirect coupling strength is purely imaginary, indicating that the indirect coupling effect is dissipative.

This LCR equivalent-circuit model offers a classical explanation for the indirect dissipative coupling in our cavity magnonic device. As all its ingredients (including the capacitors, inductors, resistors, and transmission line) are reciprocal devices, the transmission parameter of this circuit is also reciprocal. In principle, nonreciprocal behavior can be obtained in microwave circuits if a component contains either anisotropic materials or active devices [48].

-
- [1] M. H. Devoret and R. J. Schoelkopf, Superconducting circuits for quantum information: An outlook, *Science* **339**, 1169 (2013).
 - [2] P. Lodahl, S. Mahmoodian, S. Stobbe, A. Rauschenbeutel, P. Schneeweiss, J. Volz, H. Pichler, and P. Zoller, Chiral quantum optics, *Nature* **541**, 473 (2017).
 - [3] J. Gorman, D. Hasko, and D. Williams, Charge-Qubit Operation of an Isolated Double Quantum Dot, *Phys. Rev. Lett.* **95**, 090502 (2005).
 - [4] G. M. Palma, K.-A. Suominen, and A. Ekert, Quantum computers and dissipation, *Proc. Math. Phys. Eng. Sci.* **452**, 567 (1996).
 - [5] Z. Zhou, S.-I. Chu, and S. Han, Quantum computing with superconducting devices: A three-level squid qubit, *Phys. Rev. B* **66**, 054527 (2002).
 - [6] M. A. Nielsen and I. L. Chuang, *Quantum Computation and Quantum Information* (Cambridge University Press, Cambridge, England, 2010).
 - [7] Y. Tabuchi, S. Ishino, A. Noguchi, T. Ishikawa, R. Yamazaki, K. Usami, and Y. Nakamura, Coherent coupling between a ferromagnetic magnon and a superconducting qubit, *Science* **349**, 405 (2015).
 - [8] Y. Tabuchi, S. Ishino, T. Ishikawa, R. Yamazaki, K. Usami, and Y. Nakamura, Hybridizing Ferromagnetic Magnons and Microwave Photons in the Quantum Limit, *Phys. Rev. Lett.* **113**, 083603 (2014).
 - [9] D. Lachance-Quirion, Y. Tabuchi, S. Ishino, A. Noguchi, T. Ishikawa, R. Yamazaki, and Y. Nakamura, Resolving quanta of collective spin excitations in a millimeter-sized ferromagnet, *Sci. Adv.* **3**, e1603150 (2017).
 - [10] C. Caloz, A. Alù, S. Tret'yakov, D. Sounas, K. Achouri, and Z.-L. Deck-Léger, Electromagnetic Nonreciprocity, *Phys. Rev. Appl.* **10**, 047001 (2018).
 - [11] C. L. Hogan, The ferromagnetic Faraday effect at microwave frequencies and its applications, *Rev. Mod. Phys.* **25**, 253 (1953).
 - [12] A. Metelmann and A. A. Clerk, Nonreciprocal Photon Transmission and Amplification via Reservoir Engineering, *Phys. Rev. X* **5**, 021025 (2015).
 - [13] A. Metelmann and A. A. Clerk, Nonreciprocal quantum interactions and devices via autonomous feedforward, *Phys. Rev. A* **95**, 013837 (2017).
 - [14] Z. Shen, Y.-L. Zhang, Y. Chen, C.-L. Zou, Y.-F. Xiao, X.-B. Zou, F.-W. Sun, G.-C. Guo, and C.-H. Dong, Experimental realization of optomechanically induced non-reciprocity, *Nat. Photonics* **10**, 657 (2016).
 - [15] F. Ruesink, M.-A. Miri, A. Alu, and E. Verhagen, Nonreciprocity and magnetic-free isolation based on optomechanical interactions, *Nat. Commun.* **7**, 13662 (2016).
 - [16] A. Kamal, J. Clarke, and M. Devoret, Noiseless non-reciprocity in a parametric active device, *Nat. Phys.* **7**, 311 (2011).
 - [17] X. Zhang, A. Galda, X. Han, D. Jin, and V. Vinokur, Broadband Nonreciprocity Enabled by Strong Coupling of Magnons and Microwave Photons, *Phys. Rev. Appl.* **13**, 044039 (2020).
 - [18] Y.-P. Wang, J. W. Rao, Y. Yang, P.-C. Xu, Y. S. Gui, B. M. Yao, J. Q. You, and C.-M. Hu, Nonreciprocity and Unidirectional Invisibility in Cavity Magnonics, *Phys. Rev. Lett.* **123**, 127202 (2019).
 - [19] Ö. O. Soykal and M. Flatté, Strong Field Interactions between a Nanomagnet and a Photonic Cavity, *Phys. Rev. Lett.* **104**, 077202 (2010).
 - [20] G. Flower, J. Bourhill, M. Goryachev, and M. E. Tobar, Broadening frequency range of a ferromagnetic axion haloscope with strongly coupled cavity-magnon polaritons, *Phys. Dark Universe* **25**, 100306 (2019).
 - [21] Y. Cao, P. Yan, H. Huebl, S. T. B. Goennenwein, and G. E. W. Bauer, Exchange magnon-polaritons in microwave cavities, *Phys. Rev. B* **91**, 094423 (2015).
 - [22] A. Niskanen, K. Harrabi, F. Yoshihara, Y. Nakamura, S. Lloyd, and J. S. Tsai, Quantum coherent tunable coupling of superconducting qubits, *Science* **316**, 723 (2007).
 - [23] B. Z. Rameshti, Y. Cao, and G. E. Bauer, Magnetic spheres in microwave cavities, *Phys. Rev. B* **91**, 214430 (2015).
 - [24] X. Zhang, C.-L. Zou, L. Jiang, and H. X. Tang, Cavity magnomechanics, *Sci. Adv.* **2**, e1501286 (2016).
 - [25] X. Zhang, C.-L. Zou, N. Zhu, F. Marquardt, L. Jiang, and H. X. Tang, Magnon dark modes and gradient memory, *Nat. Commun.* **6**, 1 (2015).
 - [26] Y.-P. Wang, G.-Q. Zhang, D. Zhang, T.-F. Li, C.-M. Hu, and J. You, Bistability of Cavity Magnon Polaritons, *Phys. Rev. Lett.* **120**, 057202 (2018).
 - [27] J. Li, S.-Y. Zhu, and G. Agarwal, Magnon-Photon-Phonon Entanglement in Cavity Magnomechanics, *Phys. Rev. Lett.* **121**, 203601 (2018).
 - [28] D. Lachance-Quirion, Y. Tabuchi, A. Gloppe, K. Usami, and Y. Nakamura, Hybrid quantum systems based on magnonics, *Appl. Phys. Express* **12**, 070101 (2019).
 - [29] H. Huebl, C. W. Zollitsch, J. Lotze, F. Hocke, M. Greifenstein, A. Marx, R. Gross, and S. T. Goennenwein, High

- Cooperativity in Coupled Microwave Resonator Ferrimagnetic Insulator Hybrids, *Phys. Rev. Lett.* **111**, 127003 (2013).
- [30] D. Zhang, X.-Q. Luo, Y.-P. Wang, T.-F. Li, and J. You, Observation of the exceptional point in cavity magnon-polaritons, *Nat. Commun.* **8**, 1368 (2017).
- [31] X. Zhang, C.-L. Zou, L. Jiang, and H. X. Tang, Strongly Coupled Magnons and Cavity Microwave Photons, *Phys. Rev. Lett.* **113**, 156401 (2014).
- [32] M. Goryachev, W. G. Farr, D. L. Creedon, Y. Fan, M. Kostylev, and M. E. Tobar, High-Cooperativity Cavity QED with Magnons at Microwave Frequencies, *Phys. Rev. Appl.* **2**, 054002 (2014).
- [33] N. Kostylev, M. Goryachev, and M. E. Tobar, Super-strong coupling of a microwave cavity to yttrium iron garnet magnons, *Appl. Phys. Lett.* **108**, 062402 (2016).
- [34] J. Bourhill, N. Kostylev, M. Goryachev, D. Creedon, and M. Tobar, Ultrahigh cooperativity interactions between magnons and resonant photons in a YIG sphere, *Phys. Rev. B* **93**, 144420 (2016).
- [35] N. Lambert, J. Haigh, S. Langenfeld, A. Doherty, and A. Ferguson, Cavity-mediated coherent coupling of magnetic moments, *Phys. Rev. A* **93**, 021803 (2016).
- [36] W. Yu, J. Wang, H. Yuan, and J. Xiao, Prediction of Attractive Level Crossing via a Dissipative Mode, *Phys. Rev. Lett.* **123**, 227201 (2019).
- [37] M. Harder, Y. Yang, B. M. Yao, C. H. Yu, J. W. Rao, Y. S. Gui, R. L. Stamps, and C.-M. Hu, Level Attraction due to Dissipative Magnon-Photon Coupling, *Phys. Rev. Lett.* **121**, 137203 (2018).
- [38] Y. Yang, J. Rao, Y. Gui, B. Yao, W. Lu, and C.-M. Hu, Control of the Magnon-Photon Level Attraction in a Planar Cavity, *Phys. Rev. Appl.* **11**, 054023 (2019).
- [39] I. Boventer, M. Kläui, R. Macêdo, and M. Weides, Steering between level repulsion and attraction: Broad tunability of two-port driven cavity magnon-polaritons, *New J. Phys.* **21**, 125001 (2019).
- [40] I. Proskurin, R. Macêdo, and R. L. Stamps, Microscopic origin of level attraction for a coupled magnon-photon system in a microwave cavity, *New J. Phys.* **21**, 095003 (2019).
- [41] P.-C. Xu, J. Rao, Y. Gui, X. Jin, and C.-M. Hu, Cavity-mediated dissipative coupling of distant magnetic moments: Theory and experiment, *Phys. Rev. B* **100**, 094415 (2019).
- [42] V. L. Grigoryan, K. Shen, and K. Xia, Synchronized spin-photon coupling in a microwave cavity, *Phys. Rev. B* **98**, 024406 (2018).
- [43] B. Bhoi, B. Kim, S.-H. Jang, J. Kim, J. Yang, Y.-J. Cho, and S.-K. Kim, Abnormal anticrossing effect in photon-magnon coupling, *Phys. Rev. B* **99**, 134426 (2019).
- [44] J. W. Rao, Y. P. Wang, Y. Yang, T. Yu, Y. S. Gui, X. L. Fan, D. S. Xue, and C.-M. Hu, Interactions between a magnon mode and a cavity photon mode mediated by traveling photons, *Phys. Rev. B* **101**, 064404 (2020).
- [45] B. Luk'yanchuk, N. I. Zheludev, S. A. Maier, N. J. Halas, P. Nordlander, H. Giessen, and C. T. Chong, The fano resonance in plasmonic nanostructures and metamaterials, *Nat. Mater.* **9**, 707 (2010).
- [46] J. Rao, S. Kaur, X. Fan, D. Xue, B. Yao, Y. Gui, and C.-M. Hu, Characterization of the non-resonant radiation damping in coupled cavity photon magnon system, *Appl. Phys. Lett.* **110**, 262404 (2017).
- [47] R. C. Dorf, *The Electrical Engineering Handbook* (CRC Press, 1993).
- [48] D. M. Pozar, *Microwave Engineering*, 4th ed. (John Wiley & Sons, New York, 2009).
- [49] S. Kaur, B. Yao, Y.-S. Gui, and C.-M. Hu, On-chip artificial magnon-polariton device for voltage control of electromagnetically induced transparency, *J. Phys. D: Appl. Phys.* **49**, 475103 (2016).